robotics

MDPI

Article

Performance Evaluation of Cable-Driven Wrench Applicators: Geometric and Experimental Analysis †

Federico Guerra [1], Edoardo Ida' [1,*], Marco Carricato [1] and Sunil Agrawal [2]

[1] Department of Industrial Engineering, University of Bologna, 40136 Bologna, Italy; marco.carricato@unibo.it (M.C.)
[2] Department of Mechanical Engineering, Columbia University, New York, NY 10027, USA; sa3077@columbia.edu
* Correspondence: edoardo.ida2@unibo.it; Tel.: +39-051-20-90530

† This paper is an extended version of the preliminary conference contribution presented in Guerra, F.; Idà, E.; Carricato, M.; Agrawal, S. Performance Analysis of Cable-Driven Wrench Applicators. In *Cable-Driven Parallel Robots—Proceedings of CableCon 2025*; Lau, D., Pott, A., Bruckmann, T., Eds.; Springer: Berlin/Heidelberg, Germany, 2025; pp. 104–116. https://doi.org/10.1007/978-3-031-94608-0_9.

Abstract

Cable-driven wrench applicators (CDWAs) are parallel robotic systems that apply controlled wrenches to the robot end-effector through cable actuation. The presented study introduces a framework for the performance evaluation of CDWAs based on dedicated metrics. It focuses on the geometric analysis of n-cable CDWAs controlling $n-2$ wrench components and on the experimental comparison of a 4-cable architecture with an 8-cable CDWA. The geometric analysis reveals intrinsic properties of the 4-cable system's tension distribution and inherent limits in achieving specific control objectives. Both simulations and experimental validation demonstrate that the 4-cable CDWA attains comparable performance in wrench control while requiring higher tensions, yet offers greater ease of use and mechanical simplicity.

Keywords: cable-driven parallel robots; rehabilitation robotics; wrench control; force control; tension distribution; performance index; experimentation

1. Introduction

Traditional cable-driven parallel robots (CDPRs) use cables arranged in a parallel topology to control the end-effector (EE) pose, whereas cable-driven wrench applicators (CDWAs) employ the same principle to apply selected forces and moments, collectively referred to as a wrench, to the EE. CDWAs combine low moving inertia, large and scalable workspaces, lightweight and easily reconfigurable mechanical hardware, and force generation that may be tailored to the user and task [1–3]. These features make them suitable for force-controlled applications, such as rehabilitation [4,5], haptics [6], training [7,8], and wearable applications [9,10] such as exoskeletons [11,12].

Although extensive research exists on workspace characterization [13–15] and performance evaluation [16,17] for position-controlled CDPRs, the analysis of redundant CDWAs, having more cables than the number of controlled wrench components, is limited [18,19]. In particular for rehabilitation applications, where accurate and selective wrench application over large workspaces and under human-induced variability is essential, a systematic, task-aware performance analysis of redundant CDWAs is still missing. Highly redundant CDWAs are usually employed due to their greater flexibility and adaptability to external

Check for updates

Received: 22 December 2025
Revised: 26 January 2026
Accepted: 30 January 2026
Published: 2 February 2026

Copyright: © 2026 by the authors. Licensee MDPI, Basel, Switzerland. This article is an open access article distributed under the terms and conditions of the Creative Commons Attribution (CC BY) license.

disturbances and user interaction, but they might also be intrusive for a user and a therapist in rehabilitation. Redundancy introduces multiple feasible solutions for cable tensions, and choosing one that ensures continuity, positivity, and bounded limits often remains an ad hoc process [20,21]. When only a subset of wrench components is controlled, detrimental uncontrolled force/moment (thereby called parasitic components) may arise. These components must be constrained and evaluated against meaningful, task-related criteria [16]. The study of task-based criteria for controller and robot architecture comparison may instead highlight that lower-redundancy CDWA may perform equally well with lower cost of the hardware. Consequently, two main gaps persist: (i) the lack of a unified approach to systematically select the tension-distribution strategy for a given architecture based on task objectives (e.g., minimizing cable tensions versus minimizing parasitic effects), and (ii) the absence of quantitative, task-level metrics to compare different architectures in terms of cable efforts and wrench quality.

This study addresses these gaps by presenting a framework based on three dedicated performance indices:

(i) The *Overall Performance Index* (OPI), which guides the selection of the most suitable tension-distribution strategy for a fixed architecture (for instance, a quadratic program minimizing either overall tension or parasitic wrench components);
(ii) The *Maximum Tension Index* (MTI) and *Maximum Parasitic Wrench Index* (MPI), which quantify cable efforts and undesired wrench effects across the workspace, thus enabling architecture comparison and task-specific evaluation.

The proposed framework is applied to a rehabilitation task, investigating whether a simplified underconstrained 4-cable system can effectively replace a conventional overconstrained 8-cable design. Building upon the preliminarily results presented in [22], this work introduces a novel geometric formulation for n-cable CDWA tension distribution and optimization, assuming $n-2$ wrench components are to be precisely controlled, such as in a 4-cable CDWA controlling planar forces. Building on [20], we derive closed-form expressions of the feasible tension sets and identify optimal solutions for two canonical objectives: minimizing overall cable tensions and minimizing parasitic wrench components. The geometric formulation highlights when these objectives align or diverge, linking analytical conditions to observable trends in performance indices (OPI, MTI, MPI) and clarifying the trade-offs inherent to underactuated architectures. Finally, the paper validates the analytical findings through both simulations and experiments, confirming that the 4-cable CDWA has wrench-control performance comparable to the 8-cable architecture.

The remainder of the paper is structured as follows. Section 2 provides the tension computation model for a CDWA. Section 3 presents the optimization of the tension distribution through quadratic programming. Section 4 introduces the geometric analysis of an n-cable CDWA controlling $n-2$ wrench components. Section 5 defines the performance indices of the comparative framework, and Section 6 applies it to 4- and 8-cable CDWAs, including experimental validation. Section 7 concludes the paper and outlines directions for future work.

2. Wrench Exertion and Tension Control

A CDWA generates a target wrench at the EE by tensioning n cables attached to it. This section revises how cable tensions are responsible for wrench generation on a CDWA. In particular, it reviews how cable tensions produce the desired wrench and how to compute a suitable tension distribution when only a subset of m wrench components ($m < n$) is actively controlled, while the remaining $6-m$ components are minimized or otherwise managed. Let $O(x,y,z)$ be an inertial frame and $O'(x',y',z')$ a frame rigidly attached to the EE (Figure 1). The EE pose is described by the position vector $\mathbf{p}$ in the

inertial frame and by the rotation matrix $\mathbf{R}$, here parametrized via tilt–torsion angles [23]. Each cable is modeled as a straight, massless segment guided through an eyelet at B_i, whose position vector in $O(x, y, z)$ is $\mathbf{b}_i$, and attached to the EE at A_i. The latter point is constant in the EE frame, and denoted by $\mathbf{r}'_i$, and expressed in the inertial frame as $\mathbf{a}_i = \mathbf{r}_i + \mathbf{p}$, with $\mathbf{r}_i = \mathbf{R}\mathbf{r}'_i$. The cable vector is $\mathbf{l}_i = \mathbf{b}_i - \mathbf{a}_i$ and its unit direction is $\mathbf{t}_i = \mathbf{l}_i / \|\mathbf{l}_i\|$.

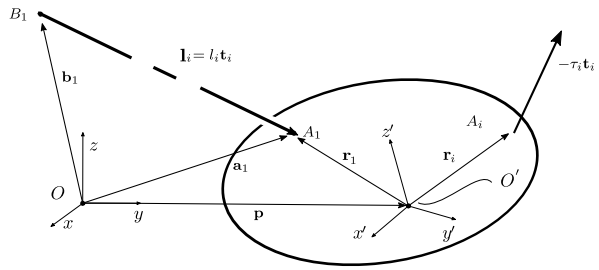

Figure 1. Geometric model of a cable-driven wrench applicator.

The wrench $\mathbf{w} = [F_x, F_y, F_z, M_x, M_y, M_z]^T \in \mathbb{R}^6$ applied to the EE relates to the cable tension array $\boldsymbol{\tau} = [\tau_1, \ldots, \tau_n]^T \in \mathbb{R}^n$ through the structure matrix $\mathbf{A} \in \mathbb{R}^{6\times n}$:

$$\mathbf{A}\,\boldsymbol{\tau} = \mathbf{w}, \tag{1}$$

where the i-th column of $\mathbf{A} = [\mathbf{a}_1, \ldots, \mathbf{a}_n]$ is

$$\mathbf{a}_i = \begin{bmatrix} \mathbf{t}_i \\ \mathbf{r}_i \times \mathbf{t}_i \end{bmatrix}, \qquad i = 1, \ldots, n. \tag{2}$$

In wrench-application problems, $\mathbf{w}$ may be either fully or partially specified. Let m be the number of components to be controlled and $s = 6 - m$. The uncontrolled components are classified as *parasitic* when they hinder performance or as *residual* when they are neutral and excluded from performance evaluation. For example, in standing-balance training, F_x and F_y are controlled to correct instability, F_z is residual, and the moments are parasitic [24]. Denote the controlled, residual, and parasitic components by $\mathbf{w}_c \in \mathbb{R}^m$, $\mathbf{w}_r \in \mathbb{R}^h$, and $\mathbf{w}_p \in \mathbb{R}^k$, with $h + k = s$. Without loss of generality, $\mathbf{w}$ can be ordered as $\mathbf{w} = [\mathbf{w}_c^\top \ \mathbf{w}_r^\top \ \mathbf{w}_p^\top]^\top$. With the corresponding partition $\mathbf{A} = [\mathbf{A}_c^\top \ \mathbf{A}_r^\top \ \mathbf{A}_p^\top]^\top$, Equation (1) becomes

$$\mathbf{A}_c\,\boldsymbol{\tau} = \mathbf{w}_c, \qquad \mathbf{A}_r\,\boldsymbol{\tau} = \mathbf{w}_r, \qquad \mathbf{A}_p\,\boldsymbol{\tau} = \mathbf{w}_p, \tag{3}$$

where $\mathbf{A}_c \in \mathbb{R}^{m\times n}$, $\mathbf{A}_r \in \mathbb{R}^{h\times n}$, and $\mathbf{A}_p \in \mathbb{R}^{k\times n}$. We refer to equalities in Equation (3) as the *controlled*, *residual*, and *parasitic* equilibrium equations, respectively. In Equation (3), the objective is to determine the tension array $\boldsymbol{\tau}$ that generates the desired wrench components $\mathbf{w}_c$ while keeping $\mathbf{w}_r$ and $\mathbf{w}_p$ within acceptable or prescribed limits. To avoid cable slackness or excessive stress, cable tensions must remain within prescribed bounds, making this a constrained optimization problem. The solution, originally presented in [25], is briefly recalled here.

We first examine the unconstrained case, temporarily neglecting physical and task-specific limits. The existence of a feasible solution depends on the number of cables and the properties of the structure matrix. Because cables can only pull, at least $(m + 1)$ cables are required to completely control m wrench components [26], implying $m \leq n - 1$. Moreover, the desired wrench array $\mathbf{w}_c$ must lie within the subspace spanned by the structure matrix

$\mathbf{A}_c$, so that $rank(\mathbf{A}_c) = m$. Under these assumptions, $\mathbf{A}_c\boldsymbol{\tau} = \mathbf{w}_c$ admits infinitely many solutions for $\boldsymbol{\tau} \in \mathbb{R}^n$, which can be expressed as in [20]:

$$\boldsymbol{\tau} = \boldsymbol{\tau}_p + \mathbf{N}\boldsymbol{\lambda}, \tag{4}$$

where $\boldsymbol{\tau}_p = \mathbf{A}_c^+\mathbf{w}_c$ is a particular solution, $\mathbf{A}_c^+ \in \mathbb{R}^{n\times m}$ is any right-inverse of $\mathbf{A}_c$ (in case the $m \times n$ matrix $\mathbf{A}_c$ has full rank m, there are infinitely many $n \times m$ matrices $\mathbf{A}_c^+$ satisfying $\mathbf{A}_c\mathbf{A}_c^+ = \mathbb{I}_m$), the columns of $\mathbf{N} \in \mathbb{R}^{n\times(n-m)}$ span a basis of the right null-space (kernel) of $\mathbf{A_c}$, and $\boldsymbol{\lambda} \in \mathbb{R}^{n-m}$ is an array of parameters determining a specific element in such a null-space. Matrix $\mathbf{N}$ can be chosen to form an orthonormal basis of $\mathbf{A}_c$ null-space, such that $\mathbf{N}^\top\mathbf{N} = \mathbb{I}_{n-m}$. Moreover, the particular solution $\boldsymbol{\tau}_p$ satisfies $\mathbf{N}^\top\boldsymbol{\tau}_p = \mathbf{0}_{n-m}$, while the homogeneous solution $\mathbf{N}\boldsymbol{\lambda}$ satisfies $\mathbf{A}_c\mathbf{N}\boldsymbol{\lambda} = \mathbf{0}_{6\times1}$ for any $\boldsymbol{\lambda}$.

Finally, Equation (4) can be substituted into the central and the rightmost equalities in Equation (3), obtaining the analytical expression of residual and parasitic components:

$$\mathbf{w}_r = \mathbf{A}_r\big(\boldsymbol{\tau}_p + \mathbf{N}\boldsymbol{\lambda}\big), \qquad \mathbf{w}_p = \mathbf{A}_p\big(\boldsymbol{\tau}_p + \mathbf{N}\boldsymbol{\lambda}\big). \tag{5}$$

The elements of $\boldsymbol{\lambda}$ are theoretically free to take any real value, leading to an *unconstrained optimization problem*, where the goal is to select an optimal $\boldsymbol{\lambda}$ to achieve a desired performance. However, in real applications, due to the presence of physical and task-specific bounds such as bounded cable tensions and parasitic wrenches, solving for $\boldsymbol{\lambda}$ requires a *constrained optimization approach*. The next section reviews the general approach of the quadratic programming (QP) formulation for solving constrained quadratic optimization problems, while Section 4 presents the geometric analysis of tension optimization for n-cable CDWAs controlling $n-2$ wrench components.

3. Tension Distribution Optimization via Quadratic Programming

As introduced in Section 2, solving the wrench-application problem for redundant CDWAs requires solving a constrained optimization, since multiple feasible solutions may exist. Among several available methods [27], we focus on quadratic programming (QP) due to its computational efficiency, smoothness of solutions, and broad adoption [4]. Two quadratic cost functions are considered to compute $\boldsymbol{\lambda}$, each highlighting key differences between CDWAs performing the same task:

QPT: *Quadratic programming for cable tension minimization*, which minimizes the square of the 2-norm of cable tensions, thereby promoting energy efficiency;

QPP: *Quadratic programming for parasitic wrench minimization*, which minimizes the square of the 2-norm of parasitic wrench components, thereby reducing undesired effects.

The cost function of QPT is derived from Equation (4) as

$$\|\boldsymbol{\tau}(\boldsymbol{\lambda})\|_2^2 = \boldsymbol{\lambda}^\top\mathbf{H}\boldsymbol{\lambda} + 2\mathbf{f}^\top\boldsymbol{\lambda} + g, \tag{6}$$

with

$$\mathbf{H} = \mathbf{N}^\top\mathbf{N} \in \mathbb{R}^{(n-m)\times(n-m)}, \quad \mathbf{f} = \mathbf{N}^\top\boldsymbol{\tau}_p \in \mathbb{R}^{(n-m)} \quad g = \boldsymbol{\tau}_p^\top\boldsymbol{\tau}_p.$$

As highlighted in Section 2, $\mathbf{N}^\top\mathbf{N} = \mathbb{I}_{n-m}$ and $\mathbf{N}^\top\boldsymbol{\tau}_p = \mathbf{0}_{n-m}$, and (6) can be rewritten as $\|\boldsymbol{\tau}(\boldsymbol{\lambda})\|_2^2 = \boldsymbol{\lambda}^\top\boldsymbol{\lambda} + g$. While g remains part of the cost function, it does not affect the optimization process as it does not depend on $\boldsymbol{\lambda}$. Thus, minimizing $\|\boldsymbol{\tau}(\boldsymbol{\lambda})\|_2^2$ is equivalent to minimizing $\boldsymbol{\lambda}^\top\boldsymbol{\lambda}$. The QPT optimization problem can be formulated as

$$\begin{aligned} \min_{\boldsymbol{\lambda}} \quad & \boldsymbol{\lambda}^\top \boldsymbol{\lambda} \\ \text{s.t.} \quad & -\begin{bmatrix} \mathbf{w}_{p,\max} \\ \mathbf{w}_{r,\max} \end{bmatrix} \leq \begin{bmatrix} \mathbf{A}_p \\ \mathbf{A}_r \end{bmatrix} \boldsymbol{\tau}(\boldsymbol{\lambda}) \leq \begin{bmatrix} \mathbf{w}_{p,\max} \\ \mathbf{w}_{r,\max} \end{bmatrix}, \\ & \boldsymbol{\tau}_{\min} \preceq \boldsymbol{\tau}(\boldsymbol{\lambda}) \preceq \boldsymbol{\tau}_{\max}. \end{aligned} \tag{7}$$

where $\preceq$ denotes element-wise inequalities, $\mathbf{w}_{p,\max}$ and $\mathbf{w}_{r,\max}$ are the arrays holding maximum values of parasitic and residual wrench components, respectively, and $\boldsymbol{\tau}_{\min}$ and $\boldsymbol{\tau}_{\max}$ are lower and upper cable tension limits, respectively.

The cost function of QPP can be found from the rightmost equality in Equation (5) as

$$\|\mathbf{w}_p(\boldsymbol{\lambda})\|_2^2 = \boldsymbol{\lambda}^\top \mathbf{L} \boldsymbol{\lambda} + 2\mathbf{p}^\top \boldsymbol{\lambda} + c, \tag{8}$$

with

$$\mathbf{L} = \mathbf{N}^\top \mathbf{A}_p^\top \mathbf{A}_p \mathbf{N} \in \mathbb{R}^{(n-m)\times(n-m)}, \quad \mathbf{p} = \mathbf{N}^\top \mathbf{A}_p^\top \mathbf{A}_p \boldsymbol{\tau}_p \in \mathbb{R}^{(n-m)}, \quad c = \boldsymbol{\tau}_p^\top \mathbf{A}_p^\top \mathbf{A}_p \boldsymbol{\tau}_p.$$

where $\mathbf{L}$ is a symmetric and positive definite matrix. Similarly to QPT, c does not depend on $\boldsymbol{\lambda}$ and can be eliminated for simplicity's sake from the optimization, yielding to the QPP optimization problem:

$$\begin{aligned} \min_{\boldsymbol{\lambda}} \quad & \boldsymbol{\lambda}^\top \mathbf{L} \boldsymbol{\lambda} + 2\mathbf{p}^\top \boldsymbol{\lambda} \\ \text{s.t.} \quad & -\mathbf{w}_{r,\max} \leq \mathbf{A}_r \boldsymbol{\tau}(\boldsymbol{\lambda}) \leq \mathbf{w}_{r,\max}, \\ & \boldsymbol{\tau}_{\min} \preceq \boldsymbol{\tau}(\boldsymbol{\lambda}) \preceq \boldsymbol{\tau}_{\max}. \end{aligned} \tag{9}$$

Once $\boldsymbol{\lambda}$ is obtained from either QPT or QPP, the corresponding tension distribution (TD) $\boldsymbol{\tau}$ is computed using Equation (4), while the residual and parasitic wrenches, $\mathbf{w}_r$ and $\mathbf{w}_p$, follow from the central and rightmost equalities in Equation (5). Numerical solvers (e.g., MATLAB 2025b `quadprog`, which implements several of the algorithms described in [28]) may provide feasible QPT/QPP solutions if one exists, but do not necessarily expose the underlying trade-offs between different control objectives. To analyze this case, we focus on a n-cable CDWA controlling $m = n - 2$ wrench components, e.g., $n = 4$ and $m = 2$. The optimization then reduces to determining $\boldsymbol{\lambda} \in \mathbb{R}^2$, enabling a geometric interpretation of the feasible tension set for both QPT and QPP. This geometric approach, originally developed for CDPRs [20], is here extended to CDWAs. Geometric analysis enables offline characterization of robot capabilities, identifying which configurations can be controlled as required.

4. Analysis of n-Cable CDWAs with $n - 2$ Controlled Wrench Components

When an n-cable CDWA has to control $m = n - 2$ wrench components, such as when a 4-cable CDWA is used to control a planar force, then $\boldsymbol{\lambda} \in \mathbb{R}^2$ and the tension allocation problem $\mathbf{A}_c\, \boldsymbol{\tau} = \mathbf{w}_c$ is underdetermined by two degrees of freedom. Once $\mathbf{w}_c$ is satisfied as per Equation (4), two independent parameters remain that redistribute tensions among the cables without altering the controlled wrench $\mathbf{w}_c$.

Formally, the solution space of Equation (4) is a two-dimensional vector subspace $\mathcal{P} \subset \mathbb{R}^2$ similar to the ones described in [20], but CDWAs also considers wrench constraints in addition to tension ones, namely

$$\mathcal{P} = \{\boldsymbol{\lambda} \in \mathbb{R}^2 \mid \boldsymbol{\tau}_{\min} \leq \boldsymbol{\tau}_p + \mathbf{N}\boldsymbol{\lambda} \leq \boldsymbol{\tau}_{\max}, \\ -\mathbf{w}_{p,\max} \leq \mathbf{A}_p(\boldsymbol{\tau}_p + \mathbf{N}\boldsymbol{\lambda}) \leq \mathbf{w}_{p,\max}, \ -\mathbf{w}_{r,\max} \leq \mathbf{A}_r(\boldsymbol{\tau}_p + \mathbf{N}\boldsymbol{\lambda}) \leq \mathbf{w}_{r,\max}\}. \quad (10)$$

The subspace $\mathcal{P}$ is referred to as the *feasible tension polygon*, as it includes all pairs $\boldsymbol{\lambda} = [\lambda_1, \lambda_2]^\top$ that, through Equation (4), generate a tension distribution $\boldsymbol{\tau}$ satisfying the limits related to cable tensions, parasitic wrenches, and residual wrenches. Rearranging the inequalities in Equation (10) gives

$$\boldsymbol{\tau}_{min} - \boldsymbol{\tau}_p \leq \mathbf{N}\boldsymbol{\lambda} \leq \boldsymbol{\tau}_{max} - \boldsymbol{\tau}_p \quad (11)$$

$$-\mathbf{w}_{p,\max} - \mathbf{A}_p\boldsymbol{\tau}_p \leq \mathbf{A}_p\mathbf{N}\boldsymbol{\lambda} \leq \mathbf{w}_{p,\max} - \mathbf{A}_p\boldsymbol{\tau}_p \quad (12)$$

$$-\mathbf{w}_{r,\max} - \mathbf{A}_r\boldsymbol{\tau}_p \leq \mathbf{A}_r\mathbf{N}\boldsymbol{\lambda} \leq \mathbf{w}_{r,\max} - \mathbf{A}_r\boldsymbol{\tau}_p \quad (13)$$

If we denote

- The i-th row of matrix $\mathbf{N}$ as $\mathbf{n}_i \in \mathbb{R}^{1\times 2}$, and the i-th element of $\boldsymbol{\tau}_p$ as $\tau_{p,i}$, for $i = 1, \ldots, n$;
- The j-th row of matrix $\mathbf{A}_p\mathbf{N}$ as $\mathbf{n}_j^p \in \mathbb{R}^{1\times 2}$, the j-th element of $\mathbf{w}_{p,\max}$ as $w_{j,\max}^p$, the j-th row of matrix $\mathbf{A}_p$ as $\mathbf{a}_j^p \in \mathbb{R}^{1\times n}$, and $w_{\tau,j}^p = \mathbf{a}_j^p\boldsymbol{\tau}_p$, for $j = 1, \ldots, k$;
- The q-th row of matrix $\mathbf{A}_r\mathbf{N}$ as $\mathbf{n}_q^r \in \mathbb{R}^{1\times 2}$, the q-th element of $\mathbf{w}_{r,\max}$ as $w_{q,\max}^r$, the q-th row of matrix $\mathbf{A}_r$ as $\mathbf{a}_q^r \in \mathbb{R}^{1\times n}$, and $w_{\tau,q}^r = \mathbf{a}_q^r\boldsymbol{\tau}_p$, for $q = 1, \ldots, h$, and $h + k = s$ as in Section 2;

Equations (11)–(13) can be explicitly written as a linear system of $2(n + s)$ inequalities:

$$\begin{array}{lll}
\mathbf{n}_1\boldsymbol{\lambda} \geq \tau_{min} - \tau_{p,1}, & \mathbf{n}_1^p\boldsymbol{\lambda} \geq -w_{1,\max}^p - w_{\tau,1}^p, & \mathbf{n}_1^r\boldsymbol{\lambda} \geq -w_{1,\max}^r - w_{\tau,1}^r, \\
\mathbf{n}_1\boldsymbol{\lambda} \leq \tau_{max} - \tau_{p,1}, & \mathbf{n}_1^p\boldsymbol{\lambda} \leq w_{1,\max}^p - w_{\tau,1}^p, & \mathbf{n}_1^r\boldsymbol{\lambda} \leq w_{1,\max}^r - w_{\tau,1}^r, \\
\mathbf{n}_2\boldsymbol{\lambda} \geq \tau_{min} - \tau_{p,2}, & \mathbf{n}_2^p\boldsymbol{\lambda} \geq -w_{2,\max}^p - w_{\tau,2}^p, & \mathbf{n}_2^r\boldsymbol{\lambda} \geq -w_{2,\max}^r - w_{\tau,2}^r, \\
\quad\vdots & \quad\vdots & \quad\vdots \\
\mathbf{n}_n\boldsymbol{\lambda} \leq \tau_{max} - \tau_{p,n}, & \mathbf{n}_k^p\boldsymbol{\lambda} \leq w_{k,\max}^p - w_{\tau,k}^p, & \mathbf{n}_h^r\boldsymbol{\lambda} \leq w_{h,\max}^r - w_{\tau,h}^r,
\end{array} \quad (14)$$

Each inequality defines a half-plane bounded by a line corresponding to values of $\boldsymbol{\lambda}$ for which one cable tension can be equal to, whether τ_{min} or τ_{max}, or alternatively lead to one of the wrench components being $\pm w_{j,\max}^p$ or $\pm w_{q,\max}^r$. The intersection of the $2(n + s)$ half-planes in Equation (14) defines the feasible tension polygon $\mathcal{P}$. For the sake of simplicity, Figure 2 represents a case where $n = 4$ and only the constraints in Equation (11) are enforced. In Figure 2a, the boundary lines, obtained by turning the inequalities into equalities, are called $L_1^{min}, L_1^{max}, L_2^{min}, \ldots, L_n^{max}$ and referred to *inequality lines*; the resulting feasible tension polygon $\mathcal{P}$ is shown in Figure 2b. A general algorithm for computing the edges of $\mathcal{P}$ in CDPRs with $n = m + 2$ cables is presented in [20]. After a finite number of iterations, the algorithm either returns the vertices of a convex feasible polygon or reports $\mathcal{P} = \emptyset$, indicating that no $\boldsymbol{\lambda} \in \mathbb{R}^2$ satisfies Equation (10). Provided that a feasible tension polygon exists, QPT and QPP can be solved exactly, as per the optimization problem formulated in Equations (7) and (9), thus allowing the key differences and similarities of the two problems to be analyzed. In the following, for illustrative sake, we will show examples computed for a 4-cable CDWA controlling planar forces F_x and F_y, thus $m = 2$, and we will only consider tension constraints, as in Equation (11).

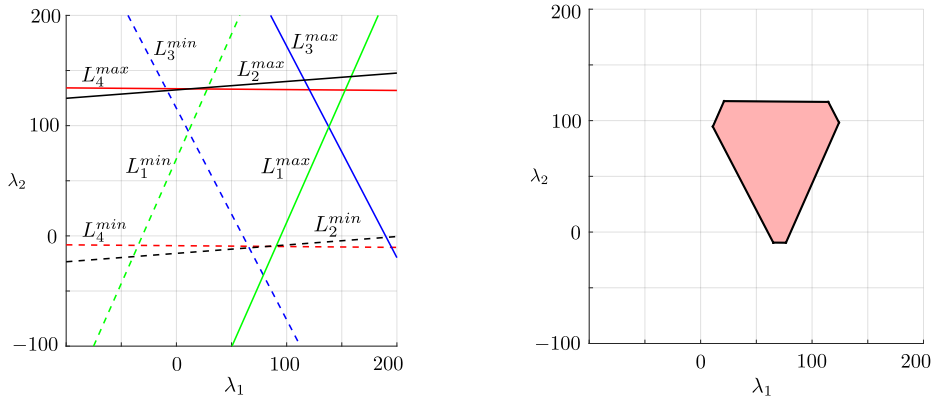

(**a**) Inequality lines (**b**) Feasible tension polygon

Figure 2. Example of feasible tension polygon of a 4-cable wrench applicator at a given pose. Colored solid and dashed lines represent upper and lower tension limits.

4.1. Algorithm for QPT Solution

Recalling Equation (7), the QPT problem can be expressed as

$$\min_{\boldsymbol{\lambda}} \boldsymbol{\lambda}^\top \boldsymbol{\lambda} \quad \text{s.t.} \quad \boldsymbol{\lambda} \in \mathcal{P}. \tag{15}$$

This is a strictly convex quadratic optimization problem with a unique global solution. Level sets are circles centered at the origin. Hence, two scenarios are to be considered:

- *Interior case.* If $\mathbf{0} \in \mathcal{P}$, then the solution to Equation (15) is the unconstrained one, namely $\boldsymbol{\lambda}^\star = \mathbf{0}$, and the subsequent tension distribution is $\boldsymbol{\tau}^\star = \boldsymbol{\tau}_p$ (Figure 3a).
- *Boundary case.* If $\mathbf{0} \notin \mathcal{P}$, the solution is the first point of contact between a circle centered in $\boldsymbol{\lambda}^\star = \mathbf{0}$ and $\mathcal{P}$ (Figure 3b,c); this results in the smallest circle centered in the unconstrained solution to Equation (15) and touching $\mathcal{P}$: the solution can be determined using the Karush–Kuhn–Tucker (KKT) conditions ([28], chapter 12) iterating over the polygon's vertices and edges.

In the following, we focus on the *Boundary case*, as the *Interior case* is straightforward: one simply substitutes $\boldsymbol{\lambda} = \mathbf{0}$ into the inequality constraints in Equation (14) to verify feasibility.

A vertex $\mathbf{v}_{ij} \in \mathcal{P}$ is obtained as the intersection of two *active-constraint* lines, derived by turning inequalities into equalities:

$$L_i : \mathbf{n}_i \boldsymbol{\lambda} = b_i - \tau_{p,i}, \qquad L_j : \ \mathbf{n}_j \boldsymbol{\lambda} = b_j - \tau_{p,j}, \tag{16}$$

$\mathbf{n}_i$ is not only the i-th row of $\mathbf{N}$, but it is also the direction normal to L_i; the scalar b_i either equals $\tau_{\min}$ or $\tau_{\max}$, depending on whether L_i enforces a lower or upper bound (and similarly for j). Since the optimal solution lies on the boundary of $\mathcal{P}$, the QPT problem can be reformulated using the Lagrangian approach [29]. The resulting Lagrangian takes different forms depending on whether the solution lies at a vertex or along an edge.

4.1.1. Vertex Optimality QPT

For each vertex candidate $\mathbf{v}_{ij}$, the Lagrangian is constructed by introducing two *active multipliers* $\mu_i, \mu_j \geq 0$ associated with the *active constrains* L_i and L_j, i.e., the constraints that are satisfied with equality at the solution:

$$\mathcal{L}(\boldsymbol{\lambda}, \mu_i, \mu_j) = \boldsymbol{\lambda}^\top \boldsymbol{\lambda} + \mu_i \left[\mathbf{n}_i \boldsymbol{\lambda} - (b_i - \tau_{p,i})\right] + \mu_j \left[\mathbf{n}_j \boldsymbol{\lambda} - (b_j - \tau_{p,j})\right]. \tag{17}$$

Stationarity with respect to $\boldsymbol{\lambda}$ implies

$$\nabla_{\boldsymbol{\lambda}} \mathcal{L} = 2\boldsymbol{\lambda} + \mathbf{n}_i^\top \mu_i + \mathbf{n}_j^\top \mu_j = \mathbf{0}. \tag{18}$$

and evaluating this latter condition at $\boldsymbol{\lambda} = \mathbf{v}_{ij}$ gives

$$\begin{bmatrix} \mathbf{n}_i^\top & \mathbf{n}_j^\top \end{bmatrix} \begin{bmatrix} \mu_i \\ \mu_j \end{bmatrix} = -2\,\mathbf{v}_{ij}. \tag{19}$$

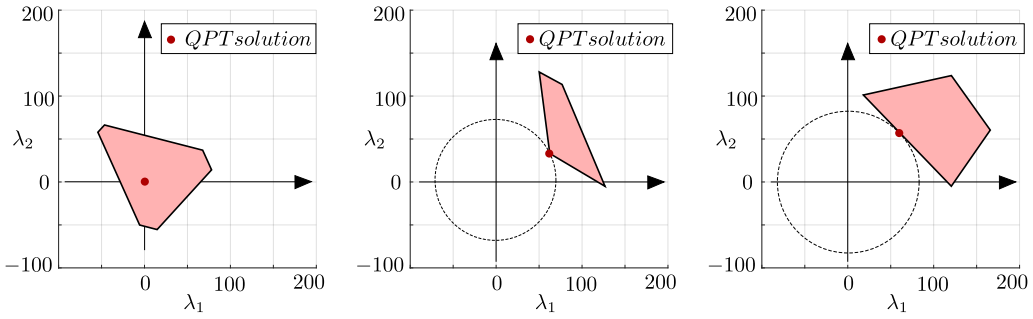

Figure 3. QPT solution cases. (**a**) $\mathbf{0} \in \mathcal{P}$. (**b**) Optimum at a vertex. (**c**) Optimum along an edge.

To determine whether a vertex satisfies the optimality conditions using the Lagrangian approach, it is essential to adopt a consistent sign convention for the normals $\mathbf{n}_i$ and $\mathbf{n}_j$ ([28], chapter 12, and [20]). We therefore introduce the *signed normals* $\boldsymbol{\alpha}_k$ $(k \in \{i, j\})$, which identify the half-plane in which each constraint is satisfied:

$$\boldsymbol{\alpha}_k \;=\; s_k\,\mathbf{n}_k^\top, \qquad s_k = \begin{cases} -1, & b_k = \tau_{\max}, \\ 1, & b_k = \tau_{\min}, \end{cases} \qquad k \in \{i, j\}. \tag{20}$$

Then the solution to (19) can be found as

$$\begin{bmatrix} \mu_i \\ \mu_j \end{bmatrix} = 2[\boldsymbol{\alpha}_i\ \boldsymbol{\alpha}_j]^{-1}\,\mathbf{v}_{ij}. \tag{21}$$

If Equation (21) yields $\mu_i \geq 0$ and $\mu_j \geq 0$, then the vertex $\mathbf{v}_{ij}$ is a KKT point and thus optimal [29] (see Figure 3b).

4.1.2. Edge Optimality QPT

If the vertex $\mathbf{v}_{ij}$ does not satisfy the KKT conditions, the search proceeds along the boundary of $\mathcal{P}$ in a prescribed direction (clockwise or counter-clockwise). Accordingly, the next candidate to evaluate is the edge lying on the the potentially active line $L_j : \mathbf{n}_j\boldsymbol{\lambda} = b_j - \tau_{p,j}$ which connects the vertex $\mathbf{v}_{ij}$ to the adjacent $\mathbf{v}_{jk} \in \mathcal{P}$. For any such edge candidate, the Lagrangian with a single active constraint L_j is

$$\mathcal{L}(\boldsymbol{\lambda}, \mu_j) = \boldsymbol{\lambda}^\top\boldsymbol{\lambda} + \mu_j\big[\mathbf{n}_j\boldsymbol{\lambda} - (b_j - \tau_{p,j})\big]. \tag{22}$$

Stationarity with respect to $\boldsymbol{\lambda}$ gives

$$\nabla_{\boldsymbol{\lambda}} \mathcal{L} = 2\boldsymbol{\lambda} + \mathbf{n}_j^\top \mu_j = \mathbf{0} \quad \Rightarrow \quad \boldsymbol{\lambda} = -\frac{\mu_j}{2}\,\mathbf{n}_j^\top. \tag{23}$$

Using the *signed normals* of Equation (20) to ensure consistency, and substituting Equation (23) into the line constraint L_j in Equation (16), allows to compute the multiplier μ_j, and ultimately the candidate solution $\boldsymbol{\lambda}$ as

$$\mu_j = \frac{2s_j\,(b_j - \tau_{p,j})}{\boldsymbol{\alpha}_j^\top \boldsymbol{\alpha}_j}, \qquad \boldsymbol{\lambda} = \frac{\mu_j}{2}\,\boldsymbol{\alpha}_j = \frac{s_j\,(b_j - \tau_{p,j})}{\|\boldsymbol{\alpha}_j\|_2^2}\,\boldsymbol{\alpha}_j. \tag{24}$$

If $\mu_j \geq 0$ and $\boldsymbol{\lambda}$ satisfies all inequalities in Equation (14), then $\boldsymbol{\lambda}$ is the optimal one. Otherwise, the candidate is discarded and the next vertices and edges of $\mathcal{P}$ are examined. An example of edge optimality is shown in Figure 3c.

4.2. Algorithm for QPP Solution

As noted in Equation (9), the QPP optimization problem is

$$\min_{\boldsymbol{\lambda}} \ \boldsymbol{\lambda}^\top \mathbf{L}\,\boldsymbol{\lambda} + 2\,\mathbf{p}^\top \boldsymbol{\lambda} \quad \text{s.t.} \quad \boldsymbol{\lambda} \in \mathcal{P}, \tag{25}$$

with $\mathbf{L} \in \mathbb{R}^{2\times 2}$ positive definite. Therefore, the level sets of this strictly convex quadratic form are ellipses with center and *unconstrained minimizer*

$$\boldsymbol{\lambda}_c = -\,\mathbf{L}^{-1}\mathbf{p}. \tag{26}$$

As in the QPT case, two scenarios arise:

- *Interior case.* If $\boldsymbol{\lambda}_c \in \mathcal{P}$, then the optimal solution is simply $\boldsymbol{\lambda}^\star = \boldsymbol{\lambda}_c$ (Figure 4a).
- *Boundary case.* If $\boldsymbol{\lambda}_c \notin \mathcal{P}$, the solution is the first point at which the ellipses expanding from the center $\boldsymbol{\lambda}_c$ touch $\mathcal{P}$ (Figure 4b,c). As in QPT, this point can be found using the KKT conditions iterating over the polygon's vertices and edges.

4.2.1. Vertex Optimality QPP

For each vertex $\mathbf{v}_{ij}$, the Lagrangian with active multipliers $\mu_i, \mu_j \geq 0$ is

$$\mathcal{L}(\boldsymbol{\lambda}, \mu_i, \mu_j) = \boldsymbol{\lambda}^\top \mathbf{L}\boldsymbol{\lambda} + 2\mathbf{p}^\top \boldsymbol{\lambda} + \mu_i[\mathbf{n}_i\boldsymbol{\lambda} - (b_i - \tau_{p,i})] + \mu_j[\mathbf{n}_j\boldsymbol{\lambda} - (b_j - \tau_{p,j})], \tag{27}$$

and stationarity with respect to $\boldsymbol{\lambda}$ requires

$$\nabla_{\boldsymbol{\lambda}}\mathcal{L}(\boldsymbol{\lambda}, \mu_i, \mu_j) = 2\mathbf{L}\boldsymbol{\lambda} + 2\mathbf{p} + \mathbf{n}_i^\top \mu_i + \mathbf{n}_j^\top \mu_j = \mathbf{0}. \tag{28}$$

Evaluating at $\boldsymbol{\lambda} = \mathbf{v}_{ij}$ yields

$$\begin{bmatrix} \mu_i \\ \mu_j \end{bmatrix} = 2[\boldsymbol{\alpha}_i \quad \boldsymbol{\alpha}_j]^{-1}(\mathbf{L}\mathbf{v}_{ij} + \mathbf{p}). \tag{29}$$

where $\boldsymbol{\alpha}_i$ and $\boldsymbol{\alpha}_j$ are the *signed normals* introduced in Equation (20). If Equation (29) yields $\mu_i \geq 0$ and $\mu_j \geq 0$, then the vertex $\mathbf{v}_{ij}$ is a QPP optimum (see Figure 4b).

4.2.2. Edge Optimality QPP

If the solution is sought on an edge, the Lagrangian with the single active multiplier μ_j is constructed similarly to the QPT case:

$$\mathcal{L}(\boldsymbol{\lambda}, \mu_j) = \boldsymbol{\lambda}^\top \mathbf{L}\boldsymbol{\lambda} + 2\mathbf{p}^\top \boldsymbol{\lambda} + \mu_j[\mathbf{n}_j\boldsymbol{\lambda} - (b_j - \tau_{p,j})]. \tag{30}$$

Stationarity with respect to $\boldsymbol{\lambda}$ gives

$$\nabla_{\boldsymbol{\lambda}} \mathcal{L}(\boldsymbol{\lambda}, \mu_j) = 2\mathbf{L}\boldsymbol{\lambda} + 2\mathbf{p} + \mathbf{n}_j^\top \mu_j = \mathbf{0} \quad \Rightarrow \quad \boldsymbol{\lambda} = \boldsymbol{\lambda}_c - \mathbf{L}^{-1}\frac{\mu_j \mathbf{n}_j^\top}{2}. \tag{31}$$

Introducing the *signed normals* of Equation (20), the result of Equation (31) is substituted into the line constraint L_j in Equation (16) to compute the multiplier μ_j and the solution candidate $\boldsymbol{\lambda}$:

$$\mu_j = \frac{2s_j(\mathbf{n}_j \mathbf{L}^{-1}\mathbf{p} + b_j - \tau_{p,j})}{\boldsymbol{\alpha}_j^\top \mathbf{L}^{-1}\boldsymbol{\alpha}_j}, \quad \boldsymbol{\lambda} = \boldsymbol{\lambda}_c + \mathbf{L}^{-1}\frac{\mu_j \boldsymbol{\alpha}_j}{2}. \tag{32}$$

As in QPT, if $\mu_j \geq 0$ and $\boldsymbol{\lambda}$ satisfies all inequalities in Equation (14), then the candidate solution is the optimal one. Otherwise, the candidate is discarded and the next vertices and edges of $\mathcal{P}$ are examined. An example of edge optimality is shown in Figure 4c.

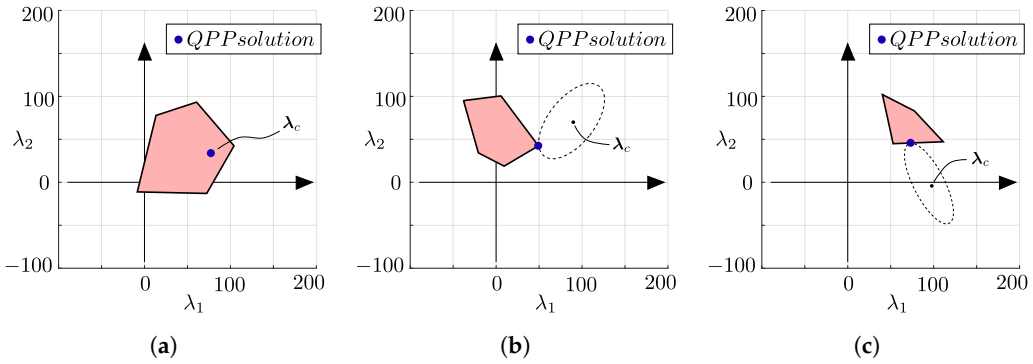

Figure 4. QPP solution cases. (**a**) $\boldsymbol{\lambda}_c \in \mathcal{P}$. (**b**) Optimum at a vertex. (**c**) Optimum along an edge.

4.3. Geometric Interpretation and Continuity

The feasible polygon $\mathcal{P}$ depends on the EE pose because both the particular solution $\boldsymbol{\tau}_p$ and the null-space basis $\mathbf{N}$ vary with position $\mathbf{p}$ and orientation $\mathbf{R}$. As a result, the half-planes of Equation (14)

$$\boldsymbol{\tau}_{\min} - \boldsymbol{\tau}_p(\mathbf{p}, \mathbf{R}) \;\leq\; \mathbf{N}(\mathbf{p}, \mathbf{R})\,\boldsymbol{\lambda} \;\leq\; \boldsymbol{\tau}_{\max} - \boldsymbol{\tau}_p(\mathbf{p}, \mathbf{R}) \tag{33}$$

also translate and rotate with the EE pose, deforming $\mathcal{P}(\mathbf{p}, \mathbf{R})$.

For QPT (Figure 5a), the level sets are circles centered at the origin, so the cost depends only on the radius. If $\boldsymbol{\lambda} = \mathbf{0} \in \mathcal{P}$, then it is the optimal solution $\boldsymbol{\lambda}^\star = \mathbf{0}$; otherwise, the optimal circle touches $\mathcal{P}$ at a vertex or along an edge (Figure 3). Since the center of the circles is always fixed at the origin, the level sets do not move with the EE pose, and $\boldsymbol{\lambda}^\star$ varies smoothly as $\mathcal{P}(\mathbf{p}, \mathbf{R})$ deforms.

For QPP (Figure 5b), the objective $\boldsymbol{\lambda}^\top \mathbf{L}\boldsymbol{\lambda} + 2\mathbf{p}^\top \boldsymbol{\lambda}$ defines ellipses centered at $\boldsymbol{\lambda}_c = -\mathbf{L}^{-1}\mathbf{p}$ with semi-axes embedded in matrix $\mathbf{L}$, both of which vary with the EE pose. Thus, as the EE moves, $\mathcal{P}$, the center $\boldsymbol{\lambda}_c$, and the ellipse geometry all change, causing the optimal QPP solution to possibly shift abruptly. Figure 5c shows this case on a 4-cable simulation ($m = 2$, $n - m = 2$): smoothly varying the pose $(\mathbf{p}, \mathbf{R})$, QPT yields a continuous locus of $\boldsymbol{\lambda}$, while QPP exhibits sudden jumps caused by edge/vertex switches. That is, the optimizer may lie on one edge (or vertex) at time k and jump to a different, possibly opposite, edge (or vertex) of $\mathcal{P}$ at time $k+1$, inducing discontinuities in $\boldsymbol{\lambda}$ and the resulting tension profile.

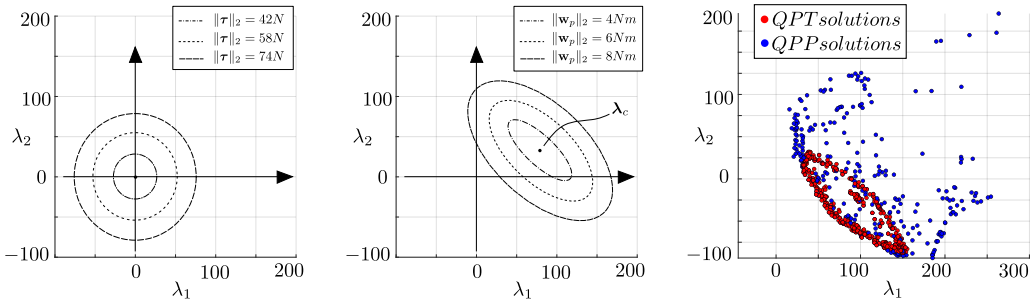

Figure 5. Comparison of QPT (**a**) and QPP (**b**) cost level sets, and variation of $\boldsymbol{\lambda}$ (**c**) with the pose of a simulated 4-cable CDWA for QPT (red) and QPP (blue).

5. Performance Metrics for Cable-Driven Wrench Applicators

In this section, we introduce three performance metrics designed for CDWAs, and also clarify their geometric meaning for 4-cable CDWAs. These indices serve two distinct purposes: (i) for a fixed robot architecture, they enable the comparison of alternative tension-distribution (TD) strategies through the *Overall Performance Index* (OPI), and (ii) once a TD has been selected, they support the evaluation of different architectures via the *Maximum Parasitic Wrench Index* (MPI) and the *Maximum Tension Index* (MTI). These indices can be used for analyzing an existing architecture, and numerically comparing its performance with another, but can be also used in a synthesis scenario, where a suitable architecture for a give application needs to be found and optimized.

All three metrics are defined locally, meaning they are computed at a specific workspace point i and over a finite set of task-relevant orientations. By sampling the workspace at N discrete positions, each associated with the same M orientations, these metrics can be examined either over the full workspace or restricted to regions of interest for the particular task. In addition, for the sake of physical consistency and practical interpretation, it is advisable to define the *controlled*, *residual*, and *parasitic* components of $\mathbf{w}$, such that $\mathbf{w}_c$ and $\mathbf{w}_p$ are a subset of forces or moments only. This choice ensures dimensional consistency in the cost functions in Equations (6) and (8) as well as in the associated performance metrics. To demonstrate how OPI, MTI, and MPI are computed, we provide examples using a 4-cable CDWA in which two wrench components are regulated and the remaining four are left uncontrolled. As shown in Section 4, this makes it possible to graphically visualize the underlying analysis and improve clarity.

5.1. Overall Performance Index (OPI)

The *Overall Performance Index* (OPI) is a dimensionless indicator used to compare two tension-distribution (TD) strategies in a CDWA when balancing cable effort (relevant for energy and wear) and parasitic wrench components that negatively influence task execution. In general, computing $\boldsymbol{\lambda}$ through QPT prioritizes reducing cable tensions, which can increase parasitic effects, whereas QPP aims to suppress parasitic components, often resulting in larger tensions. OPI identifies, for each sampled pose in the workspace, which TD achieves the most favorable compromise. A representative example of this trade-off is shown in Figure 6 for an exemplary 4-cable CDWA. Here, the parasitic wrench is taken as a vector of moments $\mathbf{w}_p = [M_x, M_y, M_z]^\top$. The QPT solution (red) yields the smallest tension norm $\|\boldsymbol{\tau}\|_2$ but produces a larger parasitic norm $\|\mathbf{w}_p\|_2$, whereas the QPP solution (blue) achieves the opposite effect. In this instance, QPT results in $\|\boldsymbol{\tau}\|_2 = 42\,\mathrm{N}$ and $\|\mathbf{w}_p\|_2 = 8\,\mathrm{Nm}$, while QPP gives $\|\boldsymbol{\tau}\|_2 = 74\,\mathrm{N}$ and $\|\mathbf{w}_p\|_2 = 6\,\mathrm{Nm}$.

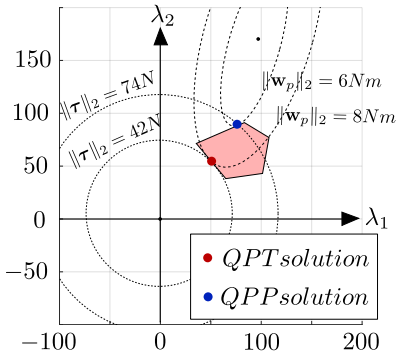

Figure 6. Comparison of QPT (red) and QPP (blue) trade-offs between overall cable tensions and parasitic effects. The pink region is the feasible polygon $\mathcal{P}$ at a given pose.

For a fixed EE position i and a set of M task-relevant orientations $\{j = 1, \ldots, M\}$, OPI aims at comparing two TDs. In this paper, we consider QPT yielding tensions $\boldsymbol{\tau}_T$ and parasitic effects $\mathbf{w}_{p_T}$, and QPP giving tensions $\boldsymbol{\tau}_P$ and parasitic effects $\mathbf{w}_{p_P}$. For each i, the worst-case RMS cable tension (reflecting how the effort is distributed across cables) and parasitic effects among the considered M orientations are

$$\boldsymbol{\tau}^*_{T,i} = \max_j \frac{\|\boldsymbol{\tau}_{T,ij}\|}{\sqrt{n}}, \qquad \boldsymbol{\tau}^*_{P,i} = \max_j \frac{\|\boldsymbol{\tau}_{P,ij}\|}{\sqrt{n}}, \tag{34}$$

$$\mathbf{w}^*_{p_{T,i}} = \max_j \|\mathbf{w}_{p_{T,ij}}\|, \qquad \mathbf{w}^*_{p_{P,i}} = \max_j \|\mathbf{w}_{p_{P,ij}}\|. \tag{35}$$

For the 4-cable CDWA, the QPT and QPP outcomes can be visualized directly as red and blue points in the $\boldsymbol{\lambda}$-plane. Neglecting the $\sqrt{n}$ factor in (34), $\boldsymbol{\tau}^*_{T,i}$ (resp. $\boldsymbol{\tau}^*_{P,i}$) equals the radius of the smallest circle centered at the origin that encloses all red (resp. blue) markers (Figure 7). In contrast, no analogous "single-plot" visualization exists for $\mathbf{w}^*_{p_{T,i}}$ and $\mathbf{w}^*_{p_{P,i}}$ because the QPP ellipses shift and deform with orientation.

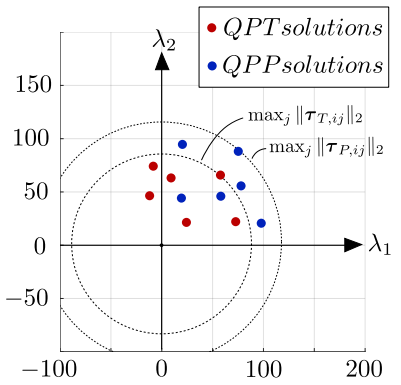

Figure 7. Comparison of QPT and QPP worst cases: $\boldsymbol{\tau}_{T,ij}$ and $\boldsymbol{\tau}_{P,ij}$ at a fixed position i across M orientations in a 4-cable CDWA. Red: $\|\boldsymbol{\tau}_T\|_2$ (QPT); blue: $\|\boldsymbol{\tau}_P\|_2$ (QPP).

The OPI at position i is defined as

$$\mathrm{OPI}_i = \Delta\boldsymbol{\tau}_i + \Delta\mathbf{w}_{p,i}, \tag{36}$$

$$\Delta\boldsymbol{\tau}_i = \frac{\boldsymbol{\tau}^*_{\mathrm{P},i} - \boldsymbol{\tau}^*_{\mathrm{T},i}}{(\boldsymbol{\tau}^*_{\mathrm{P},i} + \boldsymbol{\tau}^*_{\mathrm{T},i})/2} \cdot 100, \quad \Delta\mathbf{w}_{p,i} = \frac{\mathbf{w}^*_{p_{\mathrm{P},i}} - \mathbf{w}^*_{p_{\mathrm{T},i}}}{(\mathbf{w}^*_{p_{\mathrm{P},i}} + \mathbf{w}^*_{p_{\mathrm{T},i}})/2} \cdot 100,$$

Here, $\Delta\boldsymbol{\tau}_i$ expresses the relative variation in cable tension, computed with respect to the average value, when switching from QPT to QPP, whereas $\Delta\mathbf{w}_{p,i}$ captures the analogous change in parasitic wrench magnitude. If both terms are positive, QPT yields lower tensions and smaller parasitic effects than QPP, and the resulting OPI is positive. If both are negative, QPP performs better on both fronts. When the two terms differ in sign, a compromise arises: a positive OPI means that the improvement gained by QPP in one metric does not offset its degradation in the other, making QPT preferable overall; a negative OPI indicates the reverse. Thus, the sign of OPI provides a direct and interpretable indication of which tension-distribution strategy is more advantageous at position i.

The OPI index also presents certain limitations. Because $\Delta\boldsymbol{\tau}_i$ and $\Delta\mathbf{w}_{p,i}$ are summed without any weighting, the metric implicitly treats their contributions as equally important; this assumption may not hold for all tasks, where prioritizing one term over the other could be necessary. In future extensions, task-dependent weighting factors may be introduced to tune the relative importance of tension-related compliance versus parasitic wrench components based on patient characteristics and rehabilitation objectives. In addition, when both $\mathbf{w}^*_{p_{\mathrm{P},i}}$ and $\mathbf{w}^*_{p_{\mathrm{T},i}}$ are very small (a desirable condition), $\Delta\mathbf{w}_{p,i}$ may become ill-defined. A practical workaround is to introduce a threshold (the threshold value is task- and patient-dependent and should be selected based on patient balance and support need, rather than being treated as a fixed universal parameter): if both values fall below this bound, one can set $\Delta\mathbf{w}_{p,i} = 0$. Under this circumstance, the OPI reduces to a tension-based comparison, since the parasitic wrench is effectively negligible for both TD strategies.

Evaluating OPI throughout the workspace makes it possible to pinpoint areas where one TD strategy is clearly preferable, as its benefits exceed its drawbacks. Consequently, OPI serves as a practical criterion for choosing between two candidate TDs, whether the comparison is performed globally or restricted to task-relevant subregions. OPI is independent of the task to be performed and highlights which strategy offers the best balance between tension levels and parasitic wrench components, therefore supporting a quantifiable tuning of CDWA performance for a given task.

5.2. Maximum Tension Index (MTI) and Maximum Parasitic Wrench Index (MPI)

The *Maximum Tension Index* (MTI) and *Maximum Parasitic Wrench Index* (MPI) are intended to assess the performance of different CDWA architectures once a specific TD strategy has been chosen. MTI reflects how efficiently the system operates in terms of cable effort, while MPI indicates how well parasitic effects are suppressed during task execution.

For an EE position i and a set of M task-relevant orientations, let $\boldsymbol{\tau}_{ij}$ be the cable tensions and $\mathbf{w}_{p,ij}$ the parasitic wrench produced by the chosen TD at orientation j. We define

$$\mathrm{MTI}_i \;=\; \max_j \frac{\|\boldsymbol{\tau}_{ij}\|}{\sqrt{n}}, \qquad\qquad \mathrm{MPI}_i \;=\; \max_j \|\mathbf{w}_{p,ij}\|. \tag{37}$$

The MTI_i measures the maximum RMS value of the tension array at position i, and MPI_i measures the maximum 2-norm of the parasitic wrench, across M different orientations.

For the 4-cable CDWA, the quadratic form $\|\boldsymbol{\lambda}\|_2^2$ underlying $\|\boldsymbol{\tau}\|_2$ generates circular level sets centered at $\boldsymbol{\lambda} = \mathbf{0}$. At a fixed position i, one evaluates the chosen TD over the M task-relevant orientations, obtaining the tension array $\boldsymbol{\tau}_{ij}$ and the associated $\boldsymbol{\lambda}_{ij}$. Disregarding the normalization factor $\sqrt{n}$ in (37), MTI_i corresponds to the radius of the smallest origin-centered circle that contains all points $\boldsymbol{\lambda}_{ij}, j = 1, \ldots, M$. This geometric interpretation is shown in Figure 8.

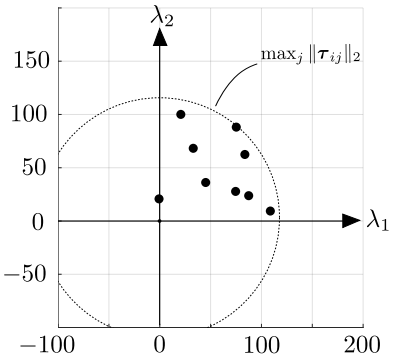

Figure 8. Planar interpretation of MTI_i. Black markers are the $\boldsymbol{\lambda}_{ij}$ solutions over M orientations at position i; MTI_i is the radius of the minimum enclosing circle centered at the origin (disregarding the $\sqrt{n}$ factor).

Conversely, as noted earlier for OPI, the parasitic wrench cost underlying QPP depends on orientation (the elliptic cost levels center and semi-axes vary with j). As a consequence, there is no orientation-independent geometric construction (analogous to the origin-centered circle used for MTI_i) that meaningfully represents MPI_i.

By evaluating MTI and MPI throughout the workspace, one obtains a quantitative performance map of the robot. These metrics are particularly useful for (i) identifying regions where cable tensions or parasitic effects become excessive; (ii) shaping task trajectories to remain within areas exhibiting low MTI and MPI; and (iii) comparing alternative robot architectures under identical workspace and task requirements. In this way, MTI and MPI provide practical tools for analyzing and refining CDWA performance, supporting both design choices and task planning, regardless of the specific task at hand.

6. Application: Comparing Two Architectures in a Rehabilitation Scenario

The *Overall Performance Index* (OPI), *Maximum Tension Index* (MTI), and *Maximum Parasitic Wrench Index* (MPI) together provide a comprehensive framework for evaluating CDWA performance. OPI captures how the selected TD strategy influences the trade-off between tension effort and parasitic effects, whereas MTI and MPI quantify the actual tension demands and parasitic wrenches once a TD has been chosen.

In this section, we apply the proposed framework to compare two *Cable-Driven Force Applicators* (CDFAs) operating on the same rehabilitation task. CDFAs represent a subclass of CDWAs used in applications where accurate force generation is essential and parasitic moments are regarded as undesirable, as noted in [30]. We examine two architectures—one using 4 cables and the other using 8—and evaluate both their relative and absolute performance under identical task conditions. The simulation results introduced in [22] are summarized for completeness' sake, and experiments on 4- and 8-cable CDFA are originally presented to confirm the simulations prediction with real robots working on a real subject.

6.1. Rehabilitation Task and System Setup

The task focuses on improving stand-balance capabilities. During the rehabilitation session, the patient stands with her/his feet in a fixed position, wears a pelvic belt (representing the robot EE) and is instructed to follow a custom-designed trajectory displayed on a screen. This trajectory challenges the patient's stability by requiring movements that push their center of mass to the limits of equilibrium. The robot provides assistance only in case of a loss of stability, by applying planar horizontal corrective forces, namely F_x and F_y,

directed towards the patient's neutral position. This control strategy is referred to as "assist-as-needed" [31], also explored in passive and dissipative devices using servo-brakes [32].

Currently, the task is carried out with an 8-cable design, implemented by the RobUST robot [24] (Figure 9a, geometric parameters in Table 1). In this study, we applied the framework proposed in Section 5 to assess the performance of a simplified four-cable design (see Figure 9b, with geometric parameters given in Table 2), where all pulleys are positioned in a single intermediate plane to improve accessibility for the physiotherapist during rehabilitation tasks.

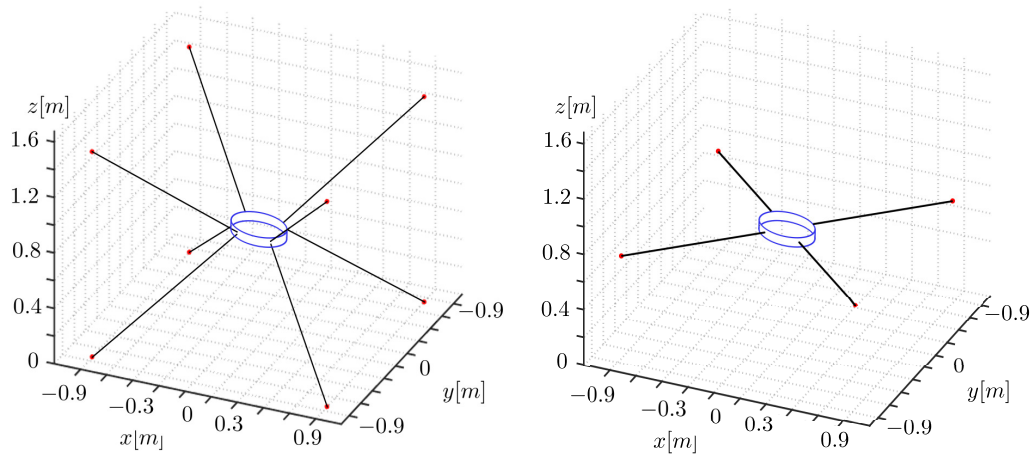

(**a**) 8-cables CDFA (RobUST). (**b**) 4-cables CDFA.

Figure 9. Architecture comparison: CDWA eyelets are in red, cables are black lines, and the cylindrical object is the EE. Reprinted with permission from [22]. 2025, Springer Nature.

Table 1. Geometrical parameters of the RobUST architecture.

i	1	2	3	4	5	6	7	8
$\mathbf{b}_i$ [m]	$\begin{bmatrix} 0.9 \\ -0.9 \\ 0 \end{bmatrix}$	$\begin{bmatrix} 0.9 \\ 0.9 \\ 0 \end{bmatrix}$	$\begin{bmatrix} -0.9 \\ -0.9 \\ 0 \end{bmatrix}$	$\begin{bmatrix} -0.9 \\ 0.9 \\ 0 \end{bmatrix}$	$\begin{bmatrix} 0.9 \\ -0.9 \\ 1.5 \end{bmatrix}$	$\begin{bmatrix} 0.9 \\ 0.9 \\ 1.5 \end{bmatrix}$	$\begin{bmatrix} -0.9 \\ -0.9 \\ 1.5 \end{bmatrix}$	$\begin{bmatrix} -0.9 \\ 0.9 \\ 1.5 \end{bmatrix}$
$\mathbf{r}'_i$ [m]	$\begin{bmatrix} 0.14 \\ -0.14 \\ -0.05 \end{bmatrix}$	$\begin{bmatrix} 0.14 \\ 0.14 \\ -0.05 \end{bmatrix}$	$\begin{bmatrix} -0.14 \\ -0.14 \\ -0.05 \end{bmatrix}$	$\begin{bmatrix} -0.14 \\ 0.14 \\ -0.05 \end{bmatrix}$	$\begin{bmatrix} 0.14 \\ -0.14 \\ 0.05 \end{bmatrix}$	$\begin{bmatrix} 0.14 \\ 0.14 \\ 0.05 \end{bmatrix}$	$\begin{bmatrix} -0.14 \\ -0.14 \\ 0.05 \end{bmatrix}$	$\begin{bmatrix} -0.14 \\ 0.14 \\ 0.05 \end{bmatrix}$

Table 2. Geometrical parameters of the 4-cable architecture.

i	1	2	3	4
$\mathbf{b}_i$ [m]	$\begin{bmatrix} 0.9 \\ -0.9 \\ 0.75 \end{bmatrix}$	$\begin{bmatrix} 0.9 \\ 0.9 \\ 0.75 \end{bmatrix}$	$\begin{bmatrix} -0.9 \\ -0.9 \\ 0.75 \end{bmatrix}$	$\begin{bmatrix} -0.9 \\ 0.9 \\ 0.75 \end{bmatrix}$
$\mathbf{r}'_i$ [m]	$\begin{bmatrix} 0.14 \\ -0.14 \\ 0 \end{bmatrix}$	$\begin{bmatrix} 0.14 \\ 0.14 \\ 0 \end{bmatrix}$	$\begin{bmatrix} -0.14 \\ -0.14 \\ 0 \end{bmatrix}$	$\begin{bmatrix} -0.14 \\ 0.14 \\ 0 \end{bmatrix}$

Overall, both the 4-cable and 8-cable CDFAs exhibit mostly positive OPI values throughout the workspace (Figure 10), indicating that QPT is generally the preferable TD strategy for both architectures. A localized region of the 8-cable workspace, however, shows negative OPI values. Because the 8-cable system has a six-dimensional null-space, only numerical TD computation methods are available in the literature, and no analytical interpretation of this behavior is currently possible. Understanding the origin of this

phenomenon remains an open direction for future investigation. For equivalent numerical reasons, computing the TD for the 4-cable systems with the geometrical methods requires on average one order of magnitude less time than computing numerically the TD for the 8-cable system (as tested on a PC running windows 11, with an intel I7-13700H CPU and 32 Gb RAM). Additional computational-time details can be found in Table 3.

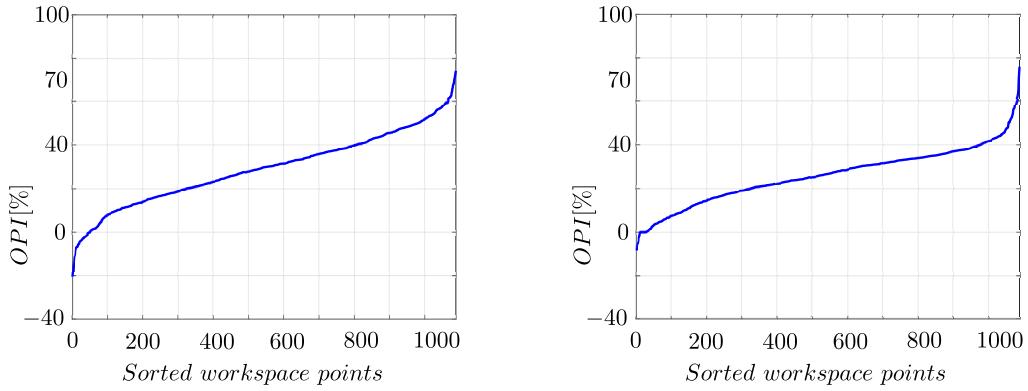

(**a**) 8-cable (**b**) 4-cable

Figure 10. Comparison of 4-cable and 8-cable OPI distribution over the workspace. Reprinted with permission from [22]. 2025, Springer Nature.

Using QPT as the selected TD for both systems, we evaluated performance through MTI and MPI. As expected, the 4-cable design shows higher MTI values across the workspace (Figure 11a–c), reflecting the increased tension required when fewer cables share the load. Conversely, its MPI values increase only when the EE moves far from the pulley plane (Figure 11b), whereas the 8-cable robot exhibits consistently higher parasitic effects throughout the workspace (Figure 11d).

Therefore, when the rehabilitation trajectory lies near the workspace center, the 4-cable architecture benefits from substantially reduced parasitic moments, better matching the task's requirements, albeit at the cost of higher cable tensions.

Table 3. Tension distribution strategies' computational times.

Number of Cables	Control Strategy	Mean Computational Time	Min Computational Time	Max Computational Time
8	QPP	3 ms	1 ms	0.8 s
8	QPT	3 ms	1 ms	0.08 s
4	QPP	0.3 ms	0.1 ms	0.05 s
4	QPT	0.3 ms	0.1 ms	0.8 s

6.2. Experimental Validation

To validate the simulation-based conclusion that an 8-cable CDFA could be replaced by a simpler 4-cable design, we conducted an experiment assessing both tension distribution and parasitic wrenches under real operating conditions. A single healthy human subject performed the rehabilitation task twice, once using the 8-cable setup and once using the 4-cable setup (Figure 12). The hardware configuration, pulley placements, and belt interfaces were reproduced to match the simulated architectures as closely as possible. In both trials, the tension distribution (TD) was computed online using the QPT method, consistent with the OPI-based recommendation from the simulation study. All task variables (trajectory, movement speed, and controlled wrench components) were held constant across the two conditions to allow a direct and fair comparison. To further standardize task

execution, the subject performed the task under real-time visual feedback. A predefined oval trajectory was displayed on a screen, together with the subject referent point (reconstructed via feedback), and a moving reference point to be followed. The task objective was to minimize spatial and temporal deviations by following the moving reference with the subject reference along the trajectory. Visual feedback was computed from a Vicon motion capture system operating at 100 Hz and was identical for both cable configurations.

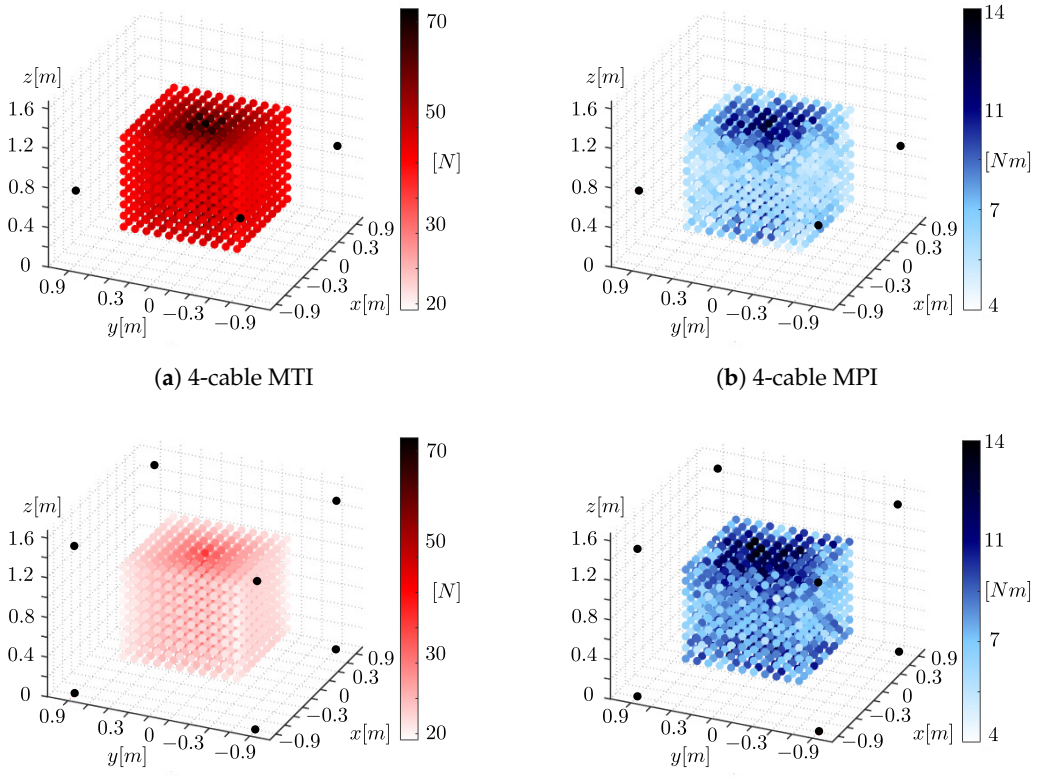

(**a**) 4-cable MTI (**b**) 4-cable MPI

(**c**) 8-cable MTI (**d**) 8-cable MPI

Figure 11. Comparison of 4-cable and 8-cable robot performances. (**a**,**b**) show the MTI and MPI for the 4-cable configuration, respectively. (**c**,**d**) present the corresponding MTI and MPI for the 8-cable configuration. Reprinted with permission from [22]. 2025, Springer Nature.

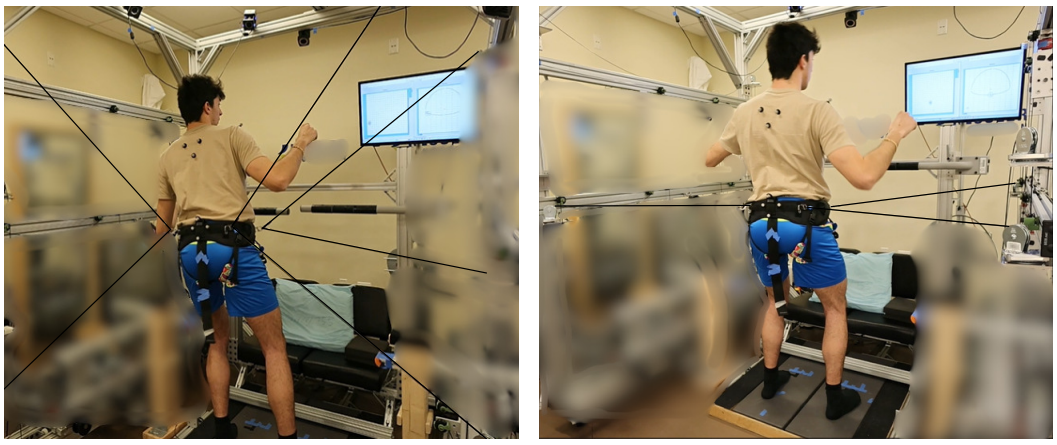

(**a**) 8-cable robot (RobUST) (**b**) 4-cable robot

Figure 12. Experimental setup for the 8-cable and 4-cable configurations.

The EE pose $(\mathbf{p}, \mathbf{R})$ and the associated structure matrices were reconstructed in real time using motion-capture data, while inline load cells recorded the cable tensions. Figure 13 shows the belt-centroid trajectories for both architectures (six repetitions per

system). At each time step, the measured pose and tension data were time-aligned, and the controlled and parasitic wrench components were obtained following the procedures described in Sections 2–4.

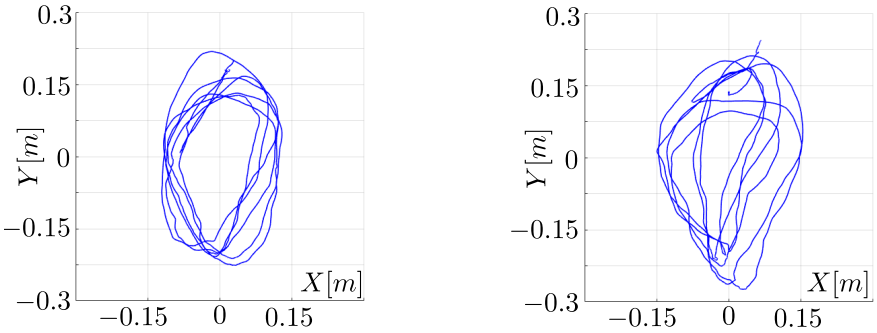

(**a**) 8-cable robot (RobUST) (**b**) 4-cable robot

Figure 13. Two-dimensional trajectories of the belt centroid. Six laps per configuration are overlaid.

In line with the framework's predictions, the 4-cable configuration demanded higher cable effort than the 8-cable one (Figure 14a). Average per-cable tensions were approximately ≈ 35–45 N for the 4-cable system and ≈ 18–30 N for the 8-cable system, with noticeably greater variability in the former (standard deviation up to ≈ 50 N versus ≈ 25 N). This behavior reflects the reduced redundancy available when only four cables must generate the same controlled wrench subset.

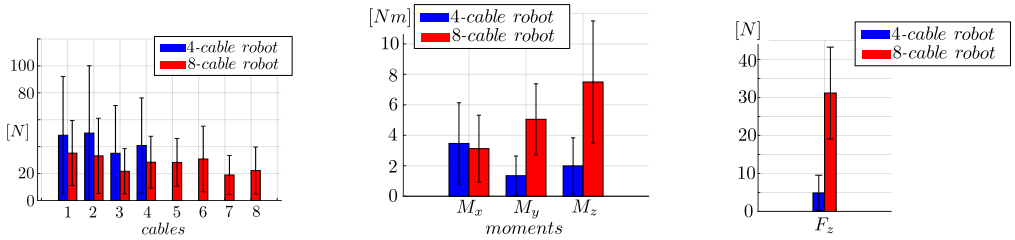

(**a**) (**b**) (**c**)

Figure 14. Experimental results. (**a**) Measured cable tensions (means and dispersion) for both configurations. (**b**) Parasitic moments (experimental). (**c**) Residual force (experimental).

The parasitic-moment measurements further reinforce the simulation trends (Figure 14b). The moment M_x was similar in both systems (mean of ≈3.7 Nm for the 4-cable and ≈3.0 Nm for the 8-cable robot), while the 4-cable configuration produced substantially lower M_y (mean ≈ 1.5 Nm compared to ≈5.0 Nm) and markedly lower M_z (mean ≈ 2.0 Nm vs. ≈7.5 Nm). The residual vertical force F_z, although not part of the controlled wrench subset, was also reduced in the 4-cable condition (mean ≈ 5 N, standard deviation ≈ 4 N) relative to the 8-cable condition (mean ≈ 30 N, standard deviation ≈ 12 N); see Figure 14c. We note that in this implementation the 4-cable pulleys were located approximately at pelvic height, favoring predominantly planar actuation aligned with the task. The 8-cable device employed multiple vertical levels, which can introduce stronger vertical coupling. Hence, differences in F_z likely arise from pulley placement as well as cable count.

To directly compare simulated and experimental behavior along the executed trajectories, we computed MTI and MPI from the measured data and compared them with their predicted values. As shown in Figures 15 and 16, the 8-cable system shows close correspondence between prediction and measurement. In the 4-cable system, simulations slightly overestimate MPI and underestimate MTI, yet the qualitative behavior and relative

ranking are preserved. Overall, the framework reproduces both the *relative* differences between the two architectures and the *absolute* magnitude of tensions and parasitic effects with good accuracy.

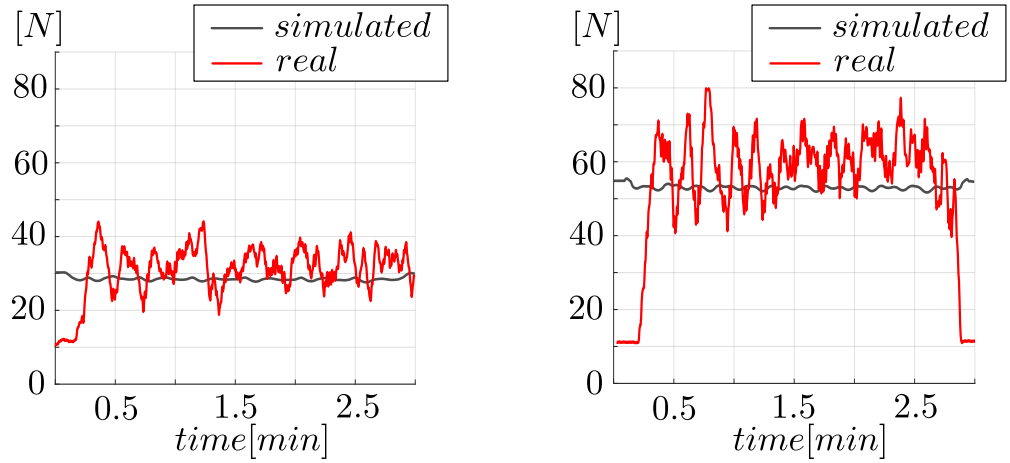

Figure 15. Comparison of simulated and measured MTI values over six laps of the experiment. The black lines represent the average simulated MTI values, while the red lines indicate the instantaneous values of the real MTIs. (**a**) MTI for the 8-Cable robot (RobUST). (**b**) MTI for the 4-cable robot.

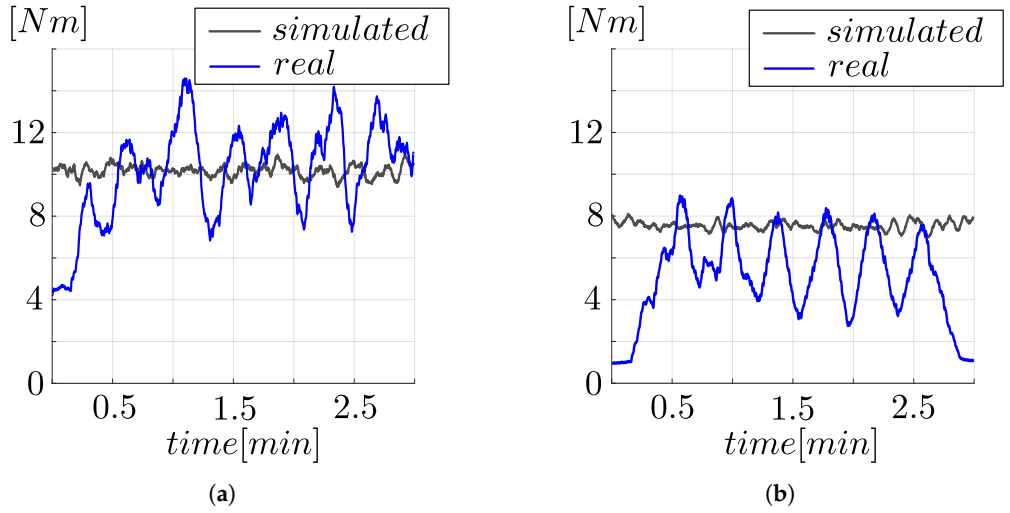

Figure 16. Comparison of simulated and measured MPI values over six laps of the experiment. The black lines represent the average simulated MPI values, while the red lines indicate the instantaneous values of the real MPIs. (**a**) MPI for the 8-Cable robot (RobUST). (**b**) MPI for the 4-cable robot.

7. Conclusions

This work presented a task-level evaluation framework for Cable-Driven Wrench Applicators that integrates three performance measures: the Overall Performance Index (OPI), used to select an appropriate tension-distribution strategy, and the Maximum Tension Index (MTI) and Maximum Parasitic Wrench Index (MPI), used to assess architecture behavior throughout the workspace. Together, these metrics enable feasibility analysis and design trade-offs by jointly accounting for cable effort and parasitic effects.

We applied the framework to a rehabilitation task to determine whether a simplified 4-cable device could replace a conventional 8-cable system. Simulation results showed that the 4-cable architecture can achieve wrench quality comparable to the 8-cable design along the task trajectory while keeping parasitic moments within acceptable bounds,

although at the price of higher cable tensions due to reduced redundancy. A controlled experiment replicating the simulated task and TD strategy confirmed these trends: (i) the 4-cable system produced a wrench quality similar to the 8-cable device with increased tensions, and (ii) for the tested geometry, the 4-cable configuration generated smaller parasitic moments. The experimentally derived MTI/MPI values aligned well with the corresponding simulation maps along the executed paths.

Beyond validating feasibility, this study also introduced a closed-form geometric formulation for geometrically calculating the tension distributions of n-cable CDWAs controlling $n-2$ wrench components, enabling a direct characterization of feasible tensions, the shape and evolution of the redundancy polygon, and the analytical conditions under which QPT and QPP coincide or diverge. This geometric insight clarifies the intrinsic trade-offs between cable tensions and parasitic effects of minimally redundant CDWAs, and explains why QPT yields smooth tension profiles whereas QPP may introduce discontinuities. Such analytical understanding is not currently available for systems with a higher redundancy (e.g., the 8-cable CDWA).

Overall, the results show that the simplified 4-cable architecture is feasible for a specific task and demonstrate that the proposed analysis-and-optimization framework offers reliable, task-oriented guidance for selecting TD strategies and comparing CDWA designs. While the 4-cable system operates with higher cable effort because the load is distributed over fewer actuators, it remains a mechanically simpler and more user-friendly alternative to highly redundant CDWAs. This study only explored OPI, MTI, and MPI on two architectures performing one type of task. Future studies should explore the sensitivity of these indices over different tasks where other wrench components are controlled, to more deeply substantiate their effectiveness.

Author Contributions: Conceptualization, F.G. and E.I.; methodology, F.G. and E.I.; software, F.G.; validation, F.G.; formal analysis, F.G.; investigation, F.G.; resources, M.C. and S.A.; data curation, F.G.; writing—original draft preparation, F.G. and E.I.; writing—review and editing, E.I., M.C. and S.A.; visualization, F.G.; supervision, E.I., M.C. and S.A.; project administration, E.I., M.C. and S.A.; funding acquisition, M.C. and S.A. All authors have read and agreed to the published version of the manuscript.

Funding: The research with Robotic Upright Stand Trainer (RobUST) is supported by a grant from the New York State Spinal Cord Injury Research Board (Grant C37719GG) to Columbia University. This study was also carried out within the MICS (Made in Italy—Circular and Sustainable) Extended Partnership and received funding from the European Union Next-GenerationEU (PIANO NAZIONALE DI RIPRESA E RESILIENZA (PNRR)—MISSIONE 4 COMPONENTE 2, INVESTIMENTO 1.3—D.D. 1551.11-10-2022, PE00000004).

Institutional Review Board Statement: The data collection with the cable-driven robotic device was carried out under the protocol AAAR6780 approved by Columbia University (latest approval date was 2 April 2025).

Data Availability Statement: Data will be shared upon reasonable request to the corresponding author.

Acknowledgments: During the preparation of this manuscript, the author(s) used ChatGPT-5.2 Education for the purposes of general text editing of the English language (language polishing, grammar, punctuation, and formatting). The authors have reviewed and re-edited the output and take full responsibility for the content of this publication.

Conflicts of Interest: The authors declare no conflicts of interest.

Nomenclature

Geometric symbols	
$\mathbf{p}$	*EE* position
$\mathbf{R}$	rotation matrix
$\mathbf{b}_i$	pulley position vector
$\mathbf{r}_i$	position vector of cable attachment point on the *EE*
$\mathbf{t}_i$	unit vector along the cable direction
l_i	cable length
Array dimensions	
n	number of cables
m	number of wrench components to be controlled
s	number of uncontrolled wrench components
r	number of residual wrench components
k	number of parasitic wrench components
Arrays and matrices	
$\mathbf{w}$	wrench (6×1)
$\mathbf{w}_c$	controlled wrench $(m \times 1)$
$\mathbf{w}_r$	residual wrench $(h \times 1)$
$\mathbf{w}_p$	parasitic wrench $(k \times 1)$
$\boldsymbol{\tau}$	cable-tension array $(n \times 1)$
$\mathbf{A}$	structure matrix $(6 \times n)$
$\mathbf{A}_c$	controlled structure matrix $(m \times n)$
$\mathbf{A}_r$	residual structure matrix $(h \times n)$
$\mathbf{A}_p$	parasitic structure matrix $(k \times n)$
Acronyms	
CDPRs	Cable-Driven Parallel Robots
EE	End Effector
CDWA	Cable-Driven Wrench Applicators
TD	Tension Distribution
OPI	Overall Performance Index
MTI	Maximum Tension Index
MPI	Maximum Parasitic Wrench Index
QPT	Quadratic Programming for cable Tension minimization
QPP	Quadratic Programming for Parasitic wrench minimization
CDFA	Cable-Driven Force Applicators

References

1. Shoaib, M.; Asadi, E.; Cheong, J.; Bab-Hadiashar, A. Cable Driven Rehabilitation Robots: Comparison of Applications and Control Strategies. *IEEE Access* **2021**, *9*, 110396–110420. [CrossRef]
2. Xiong, H.; Diao, X. A review of cable-driven rehabilitation devices. *Disabil. Rehabil. Assist. Technol.* **2020**, *15*, 885–897. [CrossRef]
3. Sanjuan De Caro, J.D.; Castillo-Blanco, J.D.; Charris, D.; Romero Martínez, D.J.; Rahman, M.H.; Nohra, C. Cable-Driven End-Effector Robots for Gait Rehabilitation: A Review and Future Research Directions. *Robotics* **2025**, *14*, 169. [CrossRef]
4. Mao, Y.; Agrawal, S.K. Design of a cable-driven arm exoskeleton (CAREX) for neural rehabilitation. *IEEE Trans. Robot.* **2012**, *28*, 922–931. [CrossRef]
5. Shi, K.; Song, A.; Li, Y.; Li, H.; Chen, D.; Zhu, L. A Cable-Driven Three-DOF Wrist Rehabilitation Exoskeleton with Improved Performance. *Front. Neurorobot.* **2021**, *15*, 664062. [CrossRef] [PubMed]
6. Saafi, H.; Laribi, M.A.; Zeghloul, S. Force control implementation of a haptic device for a medical use. In *Robotics and Mechatronics*; Zeghloul, S., Laribi, M.A., Gazeau, J.P., Eds.; Springer: Berlin/Heidelberg, Germany, 2016; Volume 37, pp. 143–151. [CrossRef]
7. Zitzewitz, J.V.; Rauter, G.; Steiner, R.; Brunschweiler, A.; Riener, R. A versatile wire robot concept as a haptic interface for sport simulation. In Proceedings of the IEEE International Conference on Robotics and Automation, ICRA 2009, Kobe, Japan, 12–17 May 2009. [CrossRef]
8. Dong, Z.; Luces, J.V.S.; Hirata, Y. Control and Evaluation of Body Weight Support Walker for Overground Gait Training. *IEEE Robot. Autom. Lett.* **2021**, *6*, 4632–4639. [CrossRef]

9. Khan, S.U.; Varghese, R.J.; Kassanos, P.; Farina, D.; Burdet, E. Space Physiology and Technology: Adaptations, Countermeasures, and Opportunity for Wearable Systems. *Cyborg Bionic Syst.* **2025**, 1–52. [CrossRef]
10. Venkata Sai Prathyush, I.; Ceccarelli, M.; Russo, M. Control Design for CABLEankle, a Cable Driven Manipulator for Ankle Motion Assistance. *Actuators* **2022**, *11*, 63. [CrossRef]
11. Bizhanov, D.; Ceccarelli, M.; Ozhikenov, K.; Zhetenbayev, N. Design Evolution and Experimental Validation of the AlmatyExoElbow Assisting Device. *Robotics* **2026**, *15*, 12. [CrossRef]
12. Choi, H.; Kang, B.B.; Jung, B.K.; Cho, K.J. Exo-Wrist: A Soft Tendon-Driven Wrist-Wearable Robot with Active Anchor for Dart-Throwing Motion in Hemiplegic Patients. *IEEE Robot. Autom. Lett.* **2019**, *4*, 4499–4506. [CrossRef]
13. Perreault, S.; Cardou, P.; Gosselin, C.M.; Otis, M.J.D. Geometric Determination of the Interference-Free Constant-Orientation Workspace of Parallel Cable-Driven Mechanisms. *J. Mech. Robot.* **2010**, *2*, 031016. [CrossRef]
14. Zake, Z.; Chaumette, F.; Pedemonte, N.; Caro, S. Control stability workspace for a cable-driven parallel robot controlled by visual servoing. In *Cable-Driven Parallel Robots—Proceedings of CableCon 2021*; Gouttefarde, M., Pott, A., Bruckmann, T., Eds.; Springer: Berlin/Heidelberg, Germany, 2021; pp. 284–296. [CrossRef]
15. Peng, L.; Duan, X.; Qiao, X. Force-Pose Stability Measures and Specified Stability Workspace Generation Techniques for Cable-Driven Parallel Robots. *J. Mech. Robot.* **2025**, *17*, 071012. [CrossRef]
16. Boschetti, G.; Trevisani, A. Cable robot performance evaluation by Wrench exertion capability. *Robotics* **2018**, *7*, 15. [CrossRef]
17. Li, Y.; Hu, Y.; Wang, W.; Zhao, P.; Zi, B. Uncertainty Analysis and Experimental Study of a Cable-Driven Parallel Lumbar Rehabilitation Robot Based on Evidence Theory. *J. Mech. Des.* **2026**, *148*, 033302. [CrossRef]
18. Zou, Y.; Wu, X.; Zhang, B.; Zhang, Q.; Zhang, A.; Qin, T. Stiffness analysis of parallel cable-driven upper limb rehabilitation robot. *Micromachines* **2022**, *13*, 253. [CrossRef]
19. KhalilianMotamed Bonab, A.; Chiaradia, D.; Frisoli, A.; Leonardis, D. A Framework for Modeling, Optimization, and Musculoskeletal Simulation of an Elbow–Wrist Exosuit. *Robotics* **2024**, *13*, 60. [CrossRef]
20. Gouttefarde, M.; Lamaury, J.; Reichert, C.; Bruckmann, T. A Versatile Tension Distribution Algorithm for n -DOF Parallel Robots Driven by $n+2$ Cables. *IEEE Trans. Robot.* **2015**, *31*, 1444–1457. [CrossRef]
21. Berretta, D.; Paola, V.D.; Caro, S.; Zoppi, M. Experimental validation of the analytic-centre based tension distribution algorithm for cable driven parallel robots. *Meccanica* **2025**, *60*, 3069–3081. [CrossRef]
22. Guerra, F.; Idà, E.; Carricato, M.; Agrawal, S. Performance Analysis of Cable-Driven Wrench Applicators. In *Cable-Driven Parallel Robots—Proceedings of CableCon 2025*; Lau, D., Pott, A., Bruckmann, T., Eds.; Springer: Berlin/Heidelberg, Germany, 2025; pp. 104–116. [CrossRef]
23. Bonev, I.; Gosselin, C. Analytical determination of the workspace of symmetrical spherical parallel mechanisms. *IEEE Trans. Robot.* **2006**, *22*, 1011–1017. [CrossRef]
24. Khan, M.; Luna, T.; Santamaria, V.; Omofuma, I.; Martelli, D.; Rejc, E.; Stein, J.; Harkema, S.; Agrawal, S. Stand Trainer With Applied Forces at the Pelvis and Trunk: Response to Perturbations and Assist-As-Needed Support. *IEEE Trans. Neural Syst. Rehabil. Eng.* **2019**, *27*, 1855–1864. [CrossRef]
25. Stramel, D.M.; Agrawal, S.K. Validation of a Forward Kinematics Based Controller for a mobile Tethered Pelvic Assist Device to Augment Pelvic Forces during Walking. In Proceedings of the 2020 IEEE International Conference on Robotics and Automation, ICRA2020, Virtual Conference, 31 May–31 August 2020. [CrossRef]
26. Mustafa, S.K.; Agrawal, S.K. On the Force-Closure Analysis of n-DOF Cable-Driven Open Chains Based on Reciprocal Screw Theory. *IEEE Trans. Robot.* **2012**, *28*, 22–31. [CrossRef]
27. Pott, A. *Cable-Driven Parallel Robots: Theory and Application*; Springer: Berlin/Heidelberg, Germany, 2019. [CrossRef]
28. Nocedal, J.; Wright, S.J. *Numerical Optimization*; Springer: Berlin/Heidelberg, Germany, 2006. [CrossRef]
29. Boyd, S.; Vandenberghe, L. *Convex Optimization*; Cambridge University Press: Cambridge, UK, 2004.
30. Khan, M.I.; Santamaria, V.; Kang, J.; Bradley, B.M.; Dutkowsky, J.P.; Gordon, A.M.; Agrawal, S.K. Enhancing Seated Stability Using Trunk Support Trainer (TruST). *IEEE Robot. Autom. Lett.* **2017**, *2*, 1609–1616. [CrossRef]
31. Banala, S.K.; Agrawal, S.K.; Kim, S.H.; Scholz, J.P. Novel Gait Adaptation and Neuromotor Training Results Using an Active Leg Exoskeleton. *IEEE/ASME Trans. Mechatron.* **2010**, *15*, 216–225. [CrossRef]
32. Abadi, B.N.R.; Hirata, Y. Control of planar passive wire-driven support systems using servo brakes. *Mech. Based Des. Struct. Mach.* **2023**, *51*, 3905–3921. [CrossRef]

Disclaimer/Publisher's Note: The statements, opinions and data contained in all publications are solely those of the individual author(s) and contributor(s) and not of MDPI and/or the editor(s). MDPI and/or the editor(s) disclaim responsibility for any injury to people or property resulting from any ideas, methods, instructions or products referred to in the content.